Robust Height Tracking by Proper Accounting of Nonlinearities in an Integrated UWB/MEMS-based-IMU/Baro System

Miao Zhang, Arun Vydhyanathan, Alexander Young and Henk Luinge
Xsens Technologies B.V.
Pantheon 6a, 7521 PR Enschede, The Netherlands
Email: miao.zhang@xsens.com

***Abstract*—This paper presents an integrated tracking system combining a MEMS-based-IMU, a UWB system and a barometer. The complementary features of the technologies make the integrated system provide a robust position and orientation estimate. The nonlinearity problem inherent in the strapdown integration solution is taken into account in the problem formulation and the methods. The use of the barometer and the incorporation of an EKF using a second order Taylor series approximation are shown to be effective in obtaining robust and reliable tracking estimates overall and in particular for the vertical channel.**

I. Introduction

Inertial sensors have the ability to output angular velocity and acceleration measurements at a high data rate with very short latency making them suitable for a wide variety of tracking applications in airborne & terrestrial navigation and applications related to that of human motion analysis. A tracking system relying on stand-alone inertial sensor measurements suffers from integration drifts over long periods of operation, typical errors are less than 2 m after 10 s for *micro-machined electromechanical system* (MEMS) based inertial sensors found in smartphones to approximately $1.8\,\mathrm{km\,h^{-1}}$ for *inertial navigation system* (INS) used for navigation in commercial aviation [1], [2]. Errors due to the integration drifts are much more significant and pronounced for systems with MEMS based gyroscopes compared to relatively high cost systems that use *fibre optic gyro*s (FOGs) and *ring laser gyro*s (RLGs).

It is customary to stabilize the position and orientation of the MEMS inertial sensors using different other information sources [3], [4]. *Ultra-wideband* (UWB) radio is a promising positioning system that has undergone massive research development in recent years [5], [6]. The localization is done using the parameters extracted from the signals that travel among different nodes. The UWB system uses a large bandwidth which provides high-precision positioning in the order of decimeters. However, it does not provide velocity and orientation information directly, these need to be deduced from the position estimate. Outliers resulting from the multipath and *non line of sight* (NLOS) propagation degrade the accuracy significantly. The complementary characteristics make the INS and UWB sensors suitable for integration to provide a robust tracking solution [4], [7]. The term robustness in this paper encompasses performance accuracy, tracking estimates with proper associated covariances and ability of the tracking algorithm to handle erroneous measurements like outliers, sensor signal saturation etc.

For many applications applying a trilateration-based positioning system, such as indoor localization or the *global positioning system* (GPS), *vertical dilution of precision* (VDOP) is usually larger than the horizontal components of *dilution of precision* (DOP) leading to a relatively poorer position estimate in the vertical direction [8]. The use of a MEMS-based-*inertial measurement unit* (IMU) poses an additional challenge in height tracking as the nature of inertial strapdown integration introduces a nonlinearity while rotating the accelerometer measurements resulting in a vertical position underestimation [9]. This grows quadratically in time. In a standard *extended Kalman filter* (EKF) formulation, linearization is done using a first order Taylor series approximation which is not capable of coping with this nonlinearity. Given the current quality of MEMS inertial sensing elements, this nonlinearity may cause inaccuracies in challenging situations like sensor saturation or data loss. As has been demonstrated in [10], combining a MEMS inertial sensor with a barometric altimeter has the potential to stabilize the height estimate.

The objective of this paper is to demonstrate robust and accurate tracking with emphasis on the performance in the vertical direction using an integrated UWB/MEMS-based-IMU/baro sensor unit. Another contribution of this paper is to prove the robust tracking performance in the challenging situation of signal saturation in the sensor in a loosely coupled *second order extended Kalman filter* (EKF2) framework [11], [12], [13]. This formulation enables accounting of the nonlinearity in the strapdown inertial integration modeling. The EKF2 performs a second order Taylor linearization in the Kalman filter framework. Not only does it estimate the mean of the nonlinear state, but also its associated error covariance which evolves with time. We have demonstrated in [9] that the EKF2 greatly improves the height estimate in strapdown inertial integration solution. In this paper we will demonstrate the performance of EKF2 for the integrated system with real data collected in an indoor environment.

The rest of the paper is organized as follows: section II gives an introduction of the integrated tracking system which

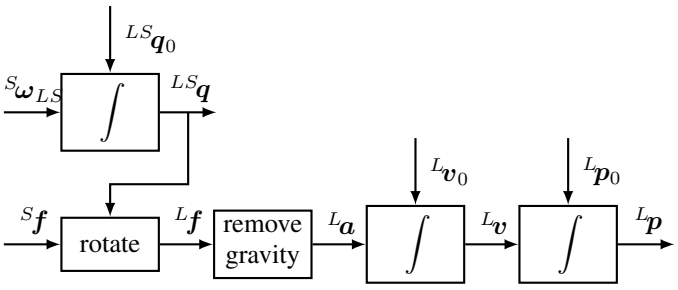

Fig. 1. Strapdown inertial integration, the orientation $^{LS}\boldsymbol{q}$ is expressed using quaternion, the velocity $^{L}\boldsymbol{v}$ and the position $^{L}\boldsymbol{p}$ are obtained by the dead reckoning from the initial condition and the inertial measurements, angular velocity $^{S}\boldsymbol{\omega}_{LS}$ and specific force $^{S}\boldsymbol{f}$.

includes the strapdown inertial integration, the UWB system and the barometer. In section III, the system model and the nonlinearity problem are formulated, section IV explains the experiment setup and the estimation results are analyzed and compared with an accurate reference system. Finally conclusions are presented in section V.

II. System Overview

The integrated system includes two components: a low-cost, low-form factor MEMS IMU consisting a *three dimensional* (3D) rate gyroscope and a 3D accelerometer which incorporates a barometer on the board, and a UWB system. In this section we will introduce each technology and their modeling for positioning purpose.

A. Strapdown inertial integration

In inertial sensors, the accelerometers measure external specific force in the imu frame (S-frame), denoted as $^{S}\boldsymbol{f}$. Gyroscopes measure the angular velocity from the S-frame to the inertial frame (I-frame) expressed in the S-frame, $^{S}\boldsymbol{\omega}_{IS}$. In order to keep the discussion simple, we apply correction terms which allow us to write the gyroscope measurement using the angular velocity from the S-frame to the local frame (L-frame) expressed in the S-frame, $^{S}\boldsymbol{\omega}_{LS}$. The inertial navigation solution calculates the current position and orientation of an object from an initial condition by integrating the information obtained from the inertial sensors which is commonly referred to as strapdown inertial integration or dead reckoning [1], as shown in Figure 1.

The inertial measurement model can then be written as

$$\boldsymbol{y}_{\mathrm{gyr}} = {}^{S}\boldsymbol{\omega}_{LS} + {}^{S}\boldsymbol{b}_{\omega} + {}^{S}\boldsymbol{e}_{\omega}, \tag{1}$$

$$\boldsymbol{y}_{\mathrm{acc}} = {}^{S}\boldsymbol{f} + {}^{S}\boldsymbol{b}_{\mathrm{a}} + {}^{S}\boldsymbol{e}_{\mathrm{a}} = {}^{SL}\boldsymbol{R}({}^{L}\boldsymbol{a} - {}^{L}\boldsymbol{g}) + {}^{S}\boldsymbol{b}_{\mathrm{a}} + {}^{S}\boldsymbol{e}_{\mathrm{a}}, \tag{2}$$

where $^{SL}\boldsymbol{R}$ denotes the rotation matrix from the L-frame to the S-frame. $^{L}\boldsymbol{a}$ represents the acceleration in the L-frame obtained by the specific force $^{L}\boldsymbol{f}$ subtracting the gravity $^{L}\boldsymbol{g}$ in the L-frame. $^{S}\boldsymbol{b}_{\omega}$ is the gyroscope bias and $^{S}\boldsymbol{b}_{\mathrm{a}}$ is the accelerometer bias. They are slow time-varying biases. $^{S}\boldsymbol{e}_{\omega}$ is the gyroscope measurement noise and $^{S}\boldsymbol{e}_{\mathrm{a}}$ is the accelerometer measurement noise. They are assumed to be zero mean *independently and identically distributed* (i.i.d.) Gaussian noises

$$^{S}\boldsymbol{e}_{\omega} \sim \mathcal{N}(\boldsymbol{0}, \boldsymbol{\Sigma}_{e_\omega}), \tag{3}$$

$$^{S}\boldsymbol{e}_{\mathrm{a}} \sim \mathcal{N}(\boldsymbol{0}, \boldsymbol{\Sigma}_{e_a}), \tag{4}$$

where $\boldsymbol{\Sigma}_{e_\omega}$ and $\boldsymbol{\Sigma}_{e_a}$ are the covariance matrix of the measurement noises of the angular velocity and the acceleration, respectively.

B. Barometer

The barometer measures the atmospheric pressure. The knowledge that air pressure decreases with increase in altitude can be used to get the height information [14]. From the pressure output of the barometer, the change in height with respect to an initial height can be obtained [10]. The absolute altitude can be calculated from the measured pressure using the international barometric formula [15]

$$h = 44330 \times (1 - (\tfrac{P}{P_0})^{\frac{1}{5.255}}), \tag{5}$$

where P is the measured pressure in Pascal, P_0 is the pressure at sea level, and the altitude h is in meters. P_0 is approximately 101.325 kPa under normal conditions, but it varies as the weather changes. Since we want to estimate the height in the L-frame and not the absolute altitude with respect to the sea level, we can model the barometer measurements as

$$y_{\mathrm{baro}} = {}^{L}p_{\mathrm{z}} + b_{\mathrm{baro}} + e_b, \tag{6}$$

where $^{L}p_{\mathrm{z}}$ is the position in z direction, i.e., height in the L-frame. b_{baro} represents the barometer baseline used to model the initial height, the calibration bias and the atmospheric pressure fluctuation due to the unstable weather. This is similar to using a reference barometer presented in [10]. The measurement noise e_b is assumed to be zero mean Gaussian noise

$$e_b \sim \mathcal{N}(0, \sigma_{e_b}^2), \tag{7}$$

which accounts for the thermal noise and the quantization noise. The typical value of σ_{e_b} for the barometer we use is approximately 0.5 m. It is apparent that the drawback of the barometer is its coarse height measurement. The advantage of using the barometer is that it provides long-term stability which can be used to limit the drift in the vertical channel estimates of the inertial sensors.

C. UWB

UWB systems have the potential to provide high-precision positioning due to their large bandwidth, which results in high time resolution. There are various parameters that can be extracted from the radio signals travelling between different nodes that can be used to calculate the node positions, such as *time of arrival* (TOA), *angle of arrival* (AOA), and *received signal strength* (RSS). The UWB system used for our experiments calculates the ranges between pairs of nodes based on the *time*

of flight (TOF) estimated by a two-way ranging protocol [6]. These ranges can be modelled as:

$$y_{\mathrm{r_i}} = \| {}^{L}\boldsymbol{p}_{\mathrm{r_i}} - {}^{L}\boldsymbol{p}\|_2 + e_r,\ i = 1, 2, ..., n, \tag{8}$$

where $\|.\|_2$ is the Euclidean distance, ${}^{L}\boldsymbol{p}$ represents the position of the target node to be tracked, and ${}^{L}\boldsymbol{p}_{\mathrm{r_i}}$ denotes the position of a reference node r_i. Note that in contrast to GPS, the ranges from a target node to the reference nodes are estimated sequentially. The reference nodes are assumed stationary with known positions. For a 3D tracking system, at least four reference nodes are required to obtain a unique position. However, if the constraint that the target node must lie on one side of the reference nodes can be applied, three reference nodes are sufficient for a 3D localization. The measurement noise e_r is assumed to be zero mean Gaussian noise

$$e_r \sim \mathcal{N}(0, \sigma_{e_r}^2). \tag{9}$$

However, when the target node moves close to the floor, walls or ceiling, due to the multipath and NLOS propagation, outliers appear that affect the range accuracy resulting in a serious degradation of range accuracy.

Another factor influencing the positioning accuracy is the *position dilution of precision* (PDOP), i.e., the geometry of the reference nodes and the target node. For a trilateration system as defined by (8), the expected positioning error consists two parts: the range measurement error σ_{e_r} and the PDOP factor

$$\mathrm{RMSE_{pos}} = \mathrm{PDOP} \cdot \sigma_{e_r}, \tag{10}$$

where $\mathrm{RMSE_{pos}}$ represents the *root mean square error* (RMSE) of the position estimate. The PDOP is then defined as

$$\mathrm{PDOP} = \frac{\sqrt{\sigma_x^2 + \sigma_y^2 + \sigma_z^2}}{\sigma_{e_r}}, \tag{11}$$

As shown in (10), a PDOP greater than one will degrade the positioning accuracy. That is, a higher value of PDOP means a poor geometry, whereas a lower value indicates a better geometry. The VDOP is calculated using (11) but only taking account of the vertical position error σ_z. The PDOP is only affected by the geometrical configuration of the reference nodes and the target node, and it can be therefore predicted for a given constellation and a specified position of the target node

$$\mathrm{PDOP} = \sqrt{\mathrm{tr}((\boldsymbol{H}^T\boldsymbol{H})^{-1})}, \tag{12}$$

where $\boldsymbol{H}$ is the Jacobian matrix of the Euclidean distance as given in (8).

III. Problem Statement

As the inertial sensor provides short-term accurate angular rate and acceleration with high data rate, it can be used to model the dynamics of the target, while the UWB range measurements and the barometer height measurements are used to correct the dead reckoning results. The hybrid tracking system can be written as a discrete-time nonlinear state space model

$$\boldsymbol{x}_{k+1} = \boldsymbol{f}(\boldsymbol{x}_k, \boldsymbol{w}_k), \tag{13}$$

$$\boldsymbol{y}_k = \boldsymbol{h}(\boldsymbol{x}_k, \boldsymbol{v}_k), \tag{14}$$

where the noises are modelled as zero mean Gaussian noises

$$\boldsymbol{w}_k \sim \mathcal{N}(\boldsymbol{0}, \boldsymbol{Q}_k), \tag{15}$$

$$\boldsymbol{v}_k \sim \mathcal{N}(\boldsymbol{0}, \boldsymbol{R}_k). \tag{16}$$

The states to be estimated are the orientation, ${}^{LS}\boldsymbol{q}$, the gyroscope bias, ${}^{S}\boldsymbol{b}_{\omega}$, the accelerometer bias, ${}^{S}\boldsymbol{b}_{\mathrm{a}}$, the velocity in the L-frame, ${}^{L}\boldsymbol{v}$, the position in the L-frame, ${}^{L}\boldsymbol{p}$, and the barometer baseline, b_{baro}. The state vector is given by

$$\boldsymbol{x} = \begin{bmatrix} {}^{LS}\boldsymbol{q} & {}^{S}\boldsymbol{b}_{\omega} & {}^{S}\boldsymbol{b}_{\mathrm{a}} & {}^{L}\boldsymbol{v} & {}^{L}\boldsymbol{p} & b_{\mathrm{baro}} \end{bmatrix}^T, \tag{17}$$

where we also estimate the barometer baseline for better tracking the barometer measurement fluctuation as the atmospheric conditions change. The system model is then given by:

System Model:

$${}^{LS}\boldsymbol{q}_{k+1} = {}^{LS}\boldsymbol{q}_k \odot \exp(\tfrac{T}{2}\, {}^{S}\boldsymbol{\omega}_{LS,k}), \tag{18a}$$

$${}^{S}\boldsymbol{b}_{\omega,k+1} = {}^{S}\boldsymbol{b}_{\omega,k} + \boldsymbol{w}_{\mathrm{b}_\omega}, \tag{18b}$$

$${}^{S}\boldsymbol{b}_{\mathrm{a},k+1} = {}^{S}\boldsymbol{b}_{\mathrm{a},k} + \boldsymbol{w}_{\mathrm{b}_\mathrm{a}}, \tag{18c}$$

$${}^{L}\boldsymbol{v}_{k+1} = {}^{L}\boldsymbol{v}_k + T\, {}^{L}\boldsymbol{a}_k, \tag{18d}$$

$${}^{L}\boldsymbol{p}_{k+1} = {}^{L}\boldsymbol{p}_k + T\, {}^{L}\boldsymbol{v}_k + \tfrac{T^2}{2}\, {}^{L}\boldsymbol{a}_k, \tag{18e}$$

$$b_{\mathrm{baro},k+1} = b_{\mathrm{baro},k} + w_{\mathrm{b_{baro}}}, \tag{18f}$$

where

$${}^{L}\boldsymbol{a}_k = {}^{LS}\boldsymbol{q}_k \odot {}^{S}\boldsymbol{f}_k \odot {}^{LS}\boldsymbol{q}_k^c + {}^{L}\boldsymbol{g}. \tag{19}$$

The orientation is represented by quaternion [16], ${}^{LS}\boldsymbol{q}$ is the rotation from the S-frame to the L-frame. (19) denotes a vector rotation using quaternion multiplication, $\odot$, and the superscript c is the quaternion conjugation operation. Here we model the gyroscope bias, accelerometer bias and the barometer baseline as random walk.

Measurement Model:

$$y_{\mathrm{r_i},k} = \| {}^{L}\boldsymbol{p}_{\mathrm{r_i}} - {}^{L}\boldsymbol{p}_k\|_2 + e_r,\ , i = 1, 2, ..., n, \tag{20}$$

$$y_{\mathrm{baro},k} = {}^{L}p_{\mathrm{z},k} + b_{\mathrm{baro},k} + e_b, \tag{21}$$

In the above system, the nonlinearity when rotating the specific force vector (19) is problematic since it always results in a downward bias in the vertical channel. As explained in [9], the probability density function of the rotated acceleration is not a Gaussian shape, but rather like an umbrella, see Figure 2. We have demonstrated this umbrella-shaped nonlinearity of the inertial strapdown integration in the previous work [9] using MEMS inertial data. As the orientation uncertainty increases, the resulting rotated acceleration will have a large bias in vertical direction. This results in a quadratically growing downward position error by double integration. It has been shown that the first order Taylor linearization does not model this bias, whereas the second order expansion models this umbrella-shaped nonlinearity more accurately. By successfully

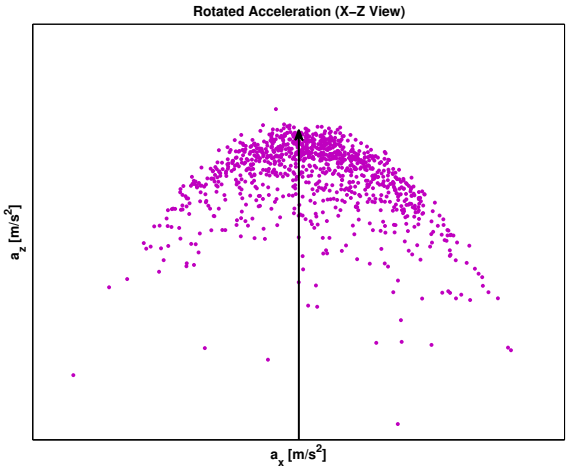

Fig. 2. Umbrella problem illustration (X-Z view) [9]. The arrow denotes an vector to be estimated, the rotated vector (the dots) due to a Gaussian distributed orientation error is distributed like an umbrella.

applying the EKF2 (prediction part) for the strapdown inertial integration, we obtain an improved height prediction as compared to a normal EKF. Therefore, applying this approach in the integration of inertial sensors with position aiding is anticipated to improve the height estimate due to a better modeling in the height direction. We will demonstrate this approach in the following section.

IV. Experimental Results

A. System setup

For the purpose of demonstration we here choose an indoor experimental setup. Five UWB reference nodes are placed in known locations inside a room with a relatively good geometric configuration.

The unit to be tracked contains a UWB target node rigidly connected to a motion tracker, i.e., the inertial sensor unit. For analysing the performance of the tracking system, we use a high-precision optical motion capture system to get an accurate and reliable position reference, with which we compare the performance of our approaches. The motion tracker data are collected at a high rate of 100 Hz, the barometer provides height information at 50 Hz, and the UWB measures the ranges in the way of 'One Shot' ranging with each reference node in turn. The range update is about 10 Hz in total, with range to each reference node estimated in turn at a rate of approximately 2 Hz as shown in Figure 3. All ranges are time-stamped using the internal clock of the target node. Figure 4 shows a typical error histogram of the range data complying to a zero mean Gaussian distribution with the standard deviation of about 0.1 m in the absence of outliers. However, the outliers happen often when the target node moves close to the floor, the ceiling, or is occluded by the body. For demonstration purposes, we remove the UWB outliers greater than $4\sigma_{e_r}$ based on the optical truth reference. We note that the problem of outlier detection itself is outside the scope of this paper. The

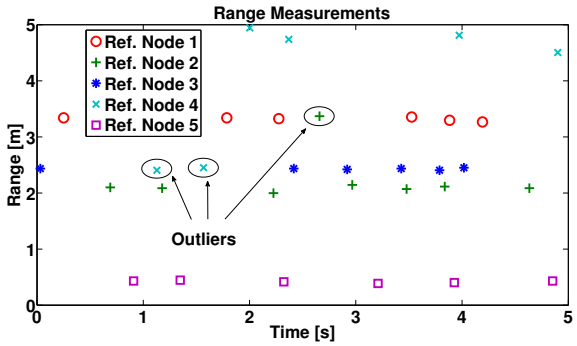

Fig. 3. Illustration of the UWB range data from five reference nodes during a static period. Some of the outliers present in the range measurements are highlighted in the figure.

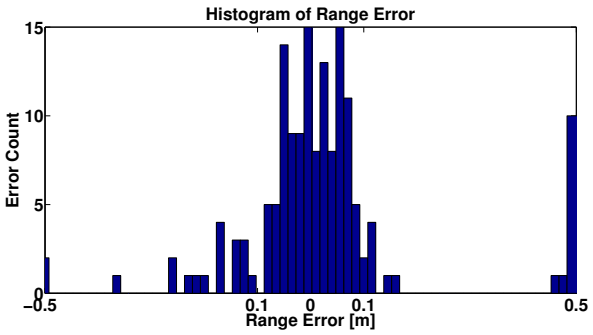

Fig. 4. Typical error histogram of the UWB range data. The outliers present in the range measurements as shown in Figure 3 make the noise distribution non-gaussian.

systems are all synchronized and aligned either in hardware or through data postprocessing.

The following two scenarios are used to demonstrate the proposed system's performance:

- Normal height tracking in human motion: the motion tracker moves randomly and the height varies in time.
- Sensor saturation: the gyroscope measurement from the motion tracker IMU saturates at times during the trial.

The following are the different integrated solutions used in the analyses:

- **EKF with baro** - the solution of the UWB, barometer and IMU in an EKF framework.
- **EKF without baro** - the solution of the UWB and IMU in an EKF framework.
- **EKF2 with baro** - is the proposed system under test. The solution of the UWB, barometer and IMU in an EKF2 framework.
- **EKF2 without baro** - the solution of the UWB and IMU in an EKF2 framework.

B. Test 1: normal height tracking in human motion

The test is to demonstrate that the proposed integrated system of the inertial sensor, the UWB system and the barometer provides smooth tracking and in particular can track the height accurately. For this test, the trajectory is chosen in the space

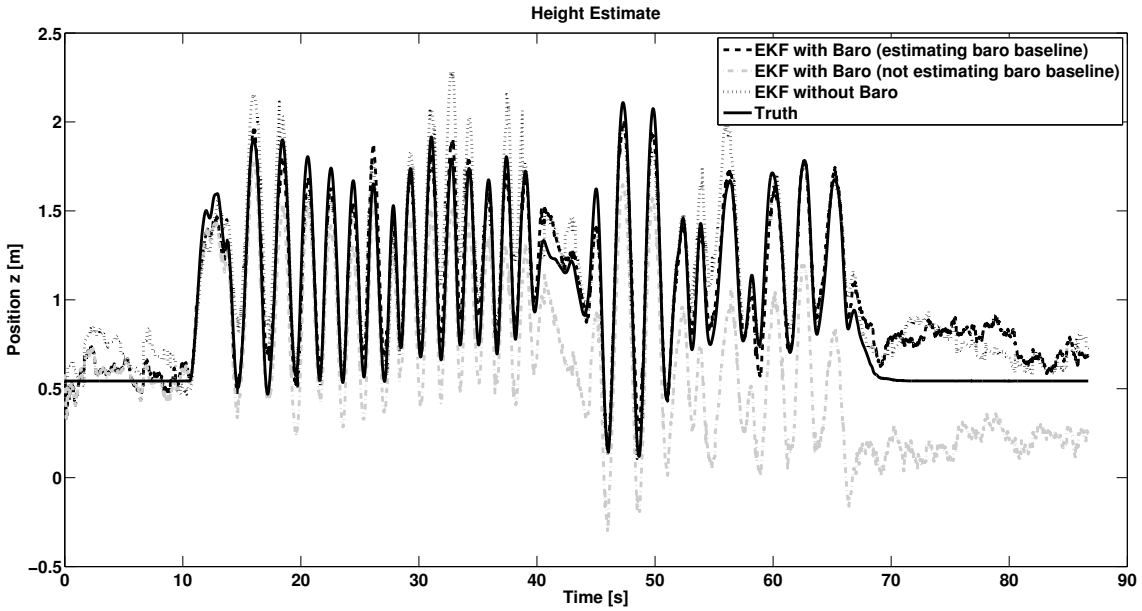

Fig. 6. Test 1: the height estimate (dashed) using EKF as compared with the true position (solid). The height estimate of an EKF without barometer (dotted) and that of an EKF with barometer but without estimating the barometer baseline (gray dash-dot) are also plotted.

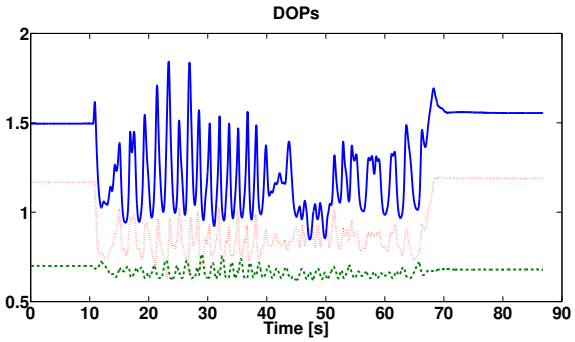

Fig. 5. DOPs during tracking, where the plots represent the DOPs in different directions (red dash-dot: x; green dashed: y; blue solid: z).

with a relatively good PDOP. As shown in Figure 5, however, the VDOP is still relatively poor being twice as bad as than that of the horizontal DOP components. Figure 6 shows the height estimate using the approach of EKF with barometer and estimating the barometer baseline, that of EKF with barometer but without estimating the barometer baseline, and that of EKF without barometer, respectively. As compared to the true position, the EKF with baro and estimating barometer baseline tracks the target continuously and accurately. As shown in Figure 3, there are usually no sufficient ranges in a single time instant and many ranging failures (gaps) in the data series. It is therefore difficult for the UWB system alone to calculate a unique position at each time and provide a continuous trajectory. In contrast, the integration of the inertial sensor and the UWB use all the information and can fill the gaps to provide smooth tracking. Moreover, the barometer adds

TABLE I
RMSES FOR TEST 1

Approaches	RMSE in x	RMSE in y	RMSE in z
EKF with Baro (baseline)	0.14 m	0.15 m	0.13 m
EKF with Baro (no baseline)	0.23 m	0.17 m	0.41 m
EKF without Baro	0.14 m	0.15 m	0.19 m

additional values to stabilize the height estimate. Comparing the height estimate applying the barometer and the estimate without the barometer, the estimation accuracy is improved. It can be seen clearly from Table I that the integration scheme including the barometer baseline as a state performs the best. The incorporation of the barometer baseline as a state further helps the tracking since an arbitrary baseline value results in height bias when the atmospheric conditions change during the trial. Without the barometer baseline as a state, the error is greater than without the barometer.

As introduced, the data rate of the barometer we used is 50 Hz. It may be a requirement to decrease the data rate to reduce the data load. Figure 7 gives the RMSEs for different barometer data rates. The height RMSE increases as the data rate decreases while the RMSEs in other channels stay at approximately the same level. It is noticed that the height RMSE increases and reaches a value in the low frequency which is close to the RMSE without using the barometer, see Table I. Without barometer the height RMSE is apparently worse than the horizontal RMSEs due to the worse VDOP. The RMSEs of the EKF2 are also plotted in Figure 7. It should be stressed that the EKF2 performs similar to the EKF here since the nonlinearity of the acceleration rotation is not prevalent for this test due to the high data rate of the inertial sensor.

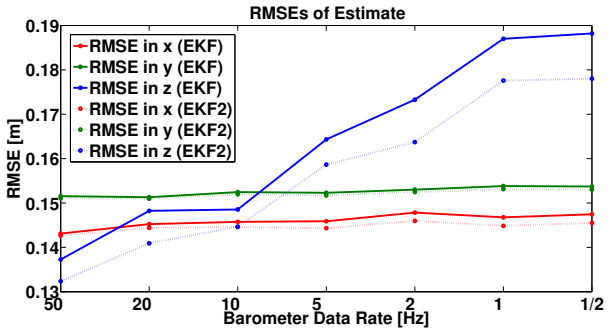

Fig. 7. The RMSEs of the EKF and EKF2 against different barometer data rates. Height estimation accuracy decreases as barometer update rate decreases. Both EKF and EKF2 achieve similar performance as there are no substantial nonlinearities during the trial.

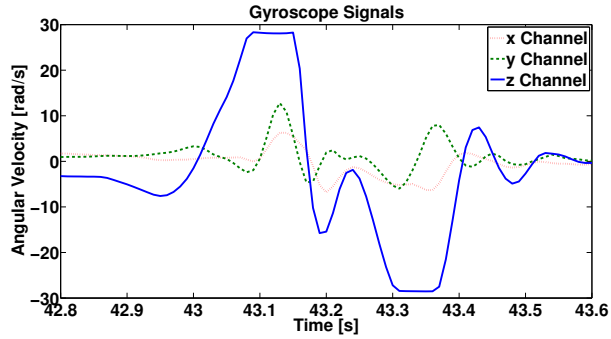

Fig. 8. Illustration of sensor saturation. The gyroscope saturates in the z channel (solid). During such a period, the angular velocity output of the gyroscope is not representative of the true motion performed.

C. Test 2: sensor saturation

This test is to prove the robust performance of the EKF2 as compared to a normal EKF in the case of high nonlinearity when the orientation uncertainty is large. Figure 8 illustrates the gyroscope saturation, where the gyroscope outputs a constant value when the sensor is rotated exceeding an angular velocity threshold, here 27.92 rad/s or 1600 °/s. That is, the gyroscope signal does not give the realistic angular velocity which is much higher than we receive from the sensor.

As derived in [9], the acceleration rotation (19) can be linearized using the 1st and 2nd order Taylor expansion. Here we split the orientation ${}^{LS}_{S}\boldsymbol{q}$ (${}^{LS}\boldsymbol{R}$) into a nominal orientation ${}^{LS}_{S}\bar{\boldsymbol{q}}$ (${}^{LS}\bar{\boldsymbol{R}}$) and an orientation error ${}^{S}\boldsymbol{\theta}$,

$$ {}^{LS}_{S}\boldsymbol{q} = {}^{LS}_{S}\bar{\boldsymbol{q}} \odot \exp(-\tfrac{1}{2}\,{}^{S}\boldsymbol{\theta}). \tag{22} $$

Given the random variables, the orientation error ${}^{S}\boldsymbol{\theta} \sim \mathcal{N}(\boldsymbol{\mu}_{s_{\boldsymbol{\theta}}}, \boldsymbol{\Sigma}_{s_{\boldsymbol{\theta}}})$, the specific force ${}^{S}\boldsymbol{f} \sim \mathcal{N}(\boldsymbol{\mu}_{s_{\boldsymbol{f}}}, \boldsymbol{\Sigma}_{s_{\boldsymbol{f}}})$ and choosing the linearization point at ${}^{S}\bar{\boldsymbol{\theta}} = \boldsymbol{\mu}_{s_{\boldsymbol{\theta}}} = 0$, we obtain the mean and covariance of the linearized function

$$ \mathrm{E}\{\boldsymbol{f}^{1st}\} = {}^{LS}\bar{\boldsymbol{R}}\boldsymbol{\mu}_{s_{\boldsymbol{f}}} + {}^{L}\boldsymbol{g}, \tag{23} $$

$$ \mathrm{Cov}\{\boldsymbol{f}^{1st}\} = [\boldsymbol{D}_{\boldsymbol{\theta}}\boldsymbol{f}]_{s_{\bar{\boldsymbol{\theta}}}} \boldsymbol{\Sigma}_{s_{\boldsymbol{\theta}}} [\boldsymbol{D}_{\boldsymbol{\theta}}\boldsymbol{f}]^{T}_{s_{\bar{\boldsymbol{\theta}}}} + {}^{LS}\bar{\boldsymbol{R}}\boldsymbol{\Sigma}_{s_{\boldsymbol{f}}}\,{}^{LS}\bar{\boldsymbol{R}}^{T}, \tag{24} $$

TABLE II
RMSES FOR TEST 2

Approaches	RMSE in x	RMSE in y	RMSE in z
EKF with Baro	0.27 m	0.19 m	0.16 m
EKF2 with Baro	0.22 m	0.15 m	0.13 m
EKF without Baro	1.23 m	1.18 m	1.35 m
EKF2 without Baro	0.43 m	0.31 m	0.54 m

and

$$ \begin{aligned} \mathrm{E}\{\boldsymbol{f}^{2nd}\} &= {}^{LS}\bar{\boldsymbol{R}}\boldsymbol{\mu}_{s_{\boldsymbol{f}}} + {}^{L}\boldsymbol{g} \\ &\quad + \tfrac{1}{2}\left[\mathrm{tr}([\boldsymbol{H}_{\boldsymbol{\theta}\boldsymbol{\theta}}\boldsymbol{f}]_{s_{\bar{\boldsymbol{\theta}},i}} \boldsymbol{\Sigma}_{s_{\boldsymbol{\theta}}})\right]_i, \end{aligned} \tag{25} $$

$$ \begin{aligned} \mathrm{Cov}\{\boldsymbol{f}^{2nd}\} &= [\boldsymbol{D}_{\boldsymbol{\theta}}\boldsymbol{f}]_{s_{\bar{\boldsymbol{\theta}}}} \boldsymbol{\Sigma}_{s_{\boldsymbol{\theta}}} [\boldsymbol{D}_{\boldsymbol{\theta}}\boldsymbol{f}]^{T}_{s_{\bar{\boldsymbol{\theta}}}} + {}^{LS}\bar{\boldsymbol{R}}\boldsymbol{\Sigma}_{s_{\boldsymbol{f}}}\,{}^{LS}\bar{\boldsymbol{R}}^{T} \\ &\quad + \tfrac{1}{2}\left[\mathrm{tr}([\boldsymbol{H}_{\boldsymbol{\theta}\boldsymbol{\theta}}\boldsymbol{f}]_{s_{\bar{\boldsymbol{\theta}},i}} \boldsymbol{\Sigma}_{s_{\boldsymbol{\theta}}} [\boldsymbol{H}_{\boldsymbol{\theta}\boldsymbol{\theta}}\boldsymbol{f}]_{s_{\bar{\boldsymbol{\theta}},j}} \boldsymbol{\Sigma}_{s_{\boldsymbol{\theta}}})\right]_{ij}, \end{aligned} \tag{26} $$

where $\mathrm{tr}(\cdot)$ is the matrix trace operation. $[\boldsymbol{x}_i]_i$ denotes a vector whose i^{th} element is $\boldsymbol{x}_i$, and $[\boldsymbol{x}_{ij}]_{ij}$ denotes a matrix whose ij^{th} element is $\boldsymbol{x}_{ij}$. $[\boldsymbol{D}_{\boldsymbol{\theta}}\boldsymbol{f}]$ denotes the Jacobian matrix and $[\boldsymbol{H}_{\boldsymbol{\theta}\boldsymbol{\theta}}\boldsymbol{f}]$ represents the Hessian matrix [17]. The details of the derivation can be found in [9]. The EKF and EKF2 provide the mean and the covariance estimate as (23) (24) and (25) (26), respectively. Comparing (23) and (25), it can be anticipated that when the additional term representing the orientation uncertainty in (25) is significant, the estimate of EKF and EKF2 will have a difference and the EKF2 can compensate the bias caused by this large orientation error, like in the situation of the gyroscope saturation. In such situation, the normal EKF only models the nonlinearity using the first order Taylor expansion, whereas the EKF2 can approximate it accurately using the second order expansion due to the bilinear nature of this nonlinearity. However, when the additional term is trivial, like in test 1, the high frequency of the motion tracker makes the linearization point ${}^{LS}\bar{\boldsymbol{R}}$ close to the true orientation, the EKF and EKF2 will output similar performance.

Figure 9 shows the height estimate obtained by the EKF and the EKF2, with and without barometer, respectively, as compared to the true position. The performance of the filters combined with the barometer is generally better than the filters without using the barometer. The EKF2s are able to provide more robust estimate as compared to the EKF. Even without the barometer aiding, the EKF2 can still converge to the true height after the saturation. Table II presents the RMSEs of different approaches, among which the EKF2 with barometer provides the best performance.

D. Test 3: UWB outage

The final test demonstrates the ability of the filters to handle an outage in the UWB aiding data. The data set from test 1 is reused, with a simulated UWB outage lasting ten seconds during a period of high dynamics. Such outages can occur in practice due to a wide variety of causes:

- occlusion of the *line of sight* (LOS) path between target and reference nodes.
- rejected measurements due to outlier detection algorithms.

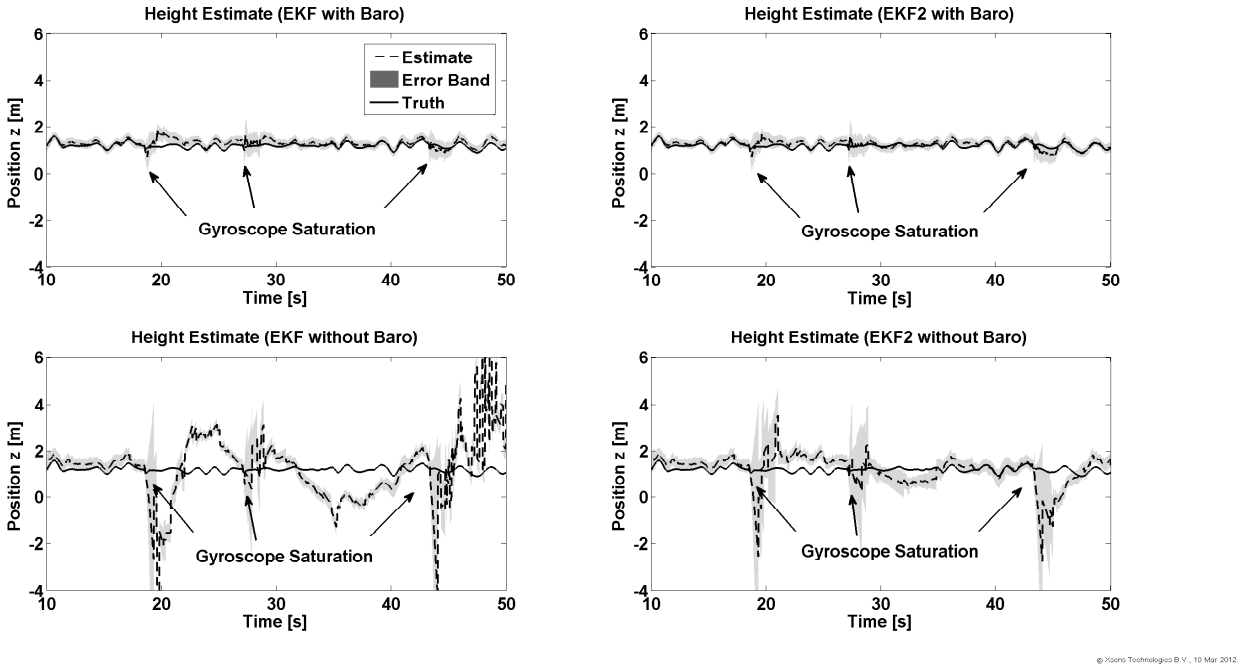

Fig. 9. Test 2: the height estimate (dashed) with the 3σ uncertainty band using different approaches as compared with the true position (solid). Comparing the upper plots with barometer data to the lower plots without, it is evident that the addition of barometer data greatly improves height estimation during gyroscopic sensor saturation events. Without barometer data the EKF is liable to diverge, while the EKF2 demonstrates its improved robustness by converging on the true solution.

- poor ranging channel access control leading to data starvation.
- movement out of range of the reference nodes.

The ability of the EKF and EKF2 filters, with and without barometer data, to track the height robustly is illustrated in Figure 10. The important difference between the EKF and EKF2 filters is highlighted by the estimated error covariance. For both filters the covariance increases during the outage as inertial integration error accumulates. For the approaches with the barometer aiding (upper figures), the covariance increasing is limited by the barometer measurement accuracy. Once UWB data are restored the EKF covariance decreases dramatically, and incorrectly, resulting in degraded performance. This is particularly evident for the EKF without barometer data where the height error jumps to over 15 m. In contrast, the EKF2 covariance decreases slower, resulting in improved integration of the noisy UWB range estimates. This clearly demonstrates the increased robustness of the EKF2 design.

The importance of the barometer in aiding height estimates is once again demonstrated for both filter types. The barometer data also reduce the error in the horizontal plane as shown by Table III.

TABLE III
RMSES FOR TEST 3

Approaches	RMSE in x	RMSE in y	RMSE in z
EKF with Baro	0.38 m	0.55 m	0.29 m
EKF2 with Baro	0.36 m	0.49 m	0.16 m
EKF without Baro	0.62 m	0.73 m	0.85 m
EKF2 without Baro	0.39 m	0.65 m	0.42 m

V. CONCLUSION

In this paper, we present an integrated tracking system consisting of a MEMS IMU, a UWB system and a barometer for robust and accurate tracking. It has been demonstrated using experiments that the incorporation of the barometer has improved the tracking in the height direction. Moreover, the nonlinearity problem of rotating the acceleration is taken account by applying an EKF2 and has been proven capable to provide more robust tracking in the challenging situations of sensor saturation and prolonged position aiding outage.

The improved robustness of the EKF2 is not without limitations however. It is still crucial to reliably detect and remove outliers from the position aiding data. The robustness of the EKF2 lies in its ability to handle aiding data outages by better modeling the nonlinearities of the strapdown inertial integration. This potentially allows the use of more conservative outlier detection algorithms with higher false positive rates.

ACKNOWLEDGMENT

The research leading to these results has received funding from the EU's Seventh Framework Programme under grant agreement no. 238710. The research has been carried out in the MC IMPULSE project: https://mcimpulse.isy.liu.se.

REFERENCES

[1] D. H. Titterton and J. L. Weston, *Strapdown Inertial Navigation Technology*. Peter Peregrinus Ltd., 1997, IEE radar, sonar, navigation and avionics series.

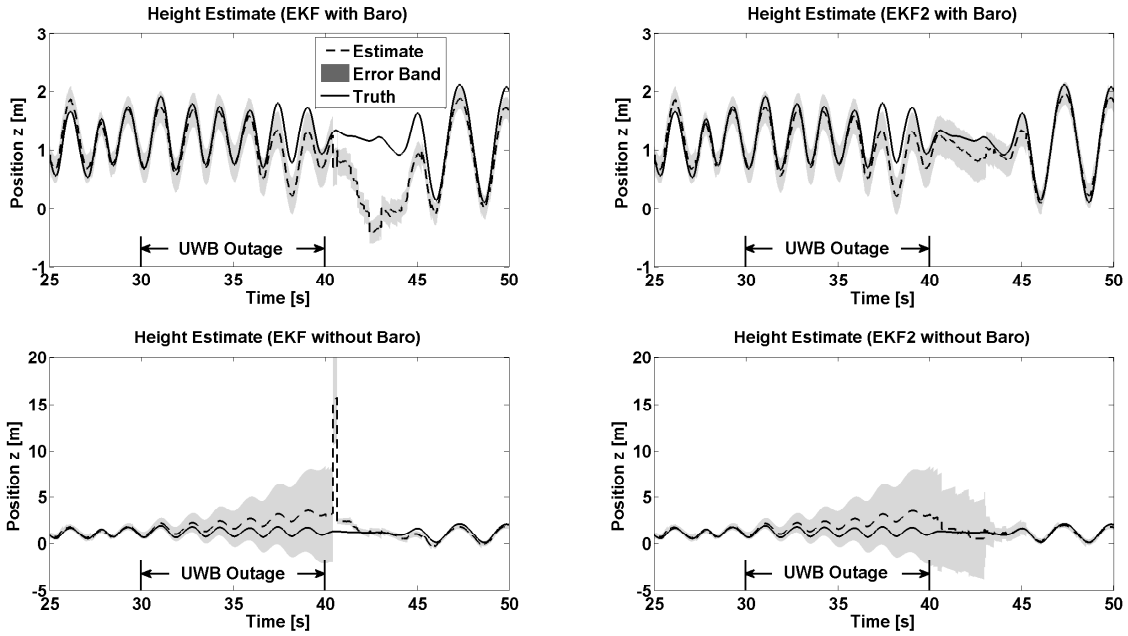

Fig. 10. Test 3: the height estimate (dashed) with the 3σ uncertainty band using different approaches as compared with the true position (solid) during UWB aiding data outage. During the outage the covariance of the state estimates increases due to integration of inertial data. For the filters aiding by the barometer in the upper figures, the covariance increasing is bounded by the barometer measurement accuracy. Once aiding data is restored, the EKF covariance rapidly decreases, meaning that incorrect Kalman gain is applied to the aiding data. This is highlighted in the lower left figure where, without barometer data, the poor EKF covariance estimate results in an unacceptable level of error.

[2] P. D. Groves, *Principles of GNSS, inertial, and multisensor integrated navigation systems*. Atrech House, 2008.

[3] A. Vydhyanathan, M. Kok, and K. L. Johnson, "A low-cost navigation system: high dynamic flight test results," in *Proc. of The European Navigation Conference on Global Navigation Satellite Systems*, Braunschweig, Germany, Oct. 2010.

[4] J. D. Hol, F. Dijkstra, H. Luinge, and T. B. Schön, "Tightly coupled UWB/IMU pose estimation," in *Proc. of IEEE International Conference on Ultra-Wideband 2009*, Vancouver, Canada, Sep. 2009, pp. 688–692.

[5] L. B. M. M. Ghavami and R. Kohno, *Ultra-wideband Signals and Systems in Communication Engineering*. John Wiley & Sons, 2007.

[6] Z. Sahinoglu, S. Gezici, and I. Guvenc, *Ultra-wideband Positioning Systems: Theoretical Limits, Ranging Algorithms, and Protocols*. Cambridge University Press, 2008.

[7] A. Vydhyanathan, H. Luinge, M. Tanigawa, F. Djikstra, M. S. Braasch, and M. Uijt de Haag, "Augmenting low-cost GPS/INS with ultra-wideband trasceivers for multi-platform relative navigation," *Proceedings of the 22^{nd} International Technical Meeting of the Satellite Division of the Institute of Navigation (ION GNSS 2009), Savannah, GA*, pp. 547–554, Sep. 2009.

[8] R. B. Langley, "Dilution of precision," *GPS World*, pp. 52–59, May 1999.

[9] M. Zhang, J. D. Hol, L. Slot, and H. Luinge, "Second order nonlinear uncertainty modeling in strapdown integration using MEMS IMUs," in *Proc. of the 14th International Conference on Information Fusion*, vol. 1, Chicago, US, Jul. 2011, pp. 1679–1685.

[10] M. Tanigawa, H. Luinge, L. Schipper, and P. Slycke, "Drift-free dynamic height sensor using MEMS IMU aided by MEMS pressure sensor," in *Proc. of 5th Workshop on Positioning, Navigation and Communication, 2008*, Hannover, Germany, Mar. 2008, pp. 191–196.

[11] F. Gustafsson, *Statistical Sensor Fusion*. Studentlitteratur, 2010.

[12] P. S. Maybeck, *Stochastic Models, Estimation, and Control*. Academic Press, 1979, vol. 2.

[13] M. Roth and F. Gustafsson, "An efficient implementation of the second order extended Kalman filter," in *Proc. of the 14th International Conference on Information Fusion*, vol. 1, Chicago, US, Jul. 2011, pp. 1913–1918.

[14] J. K. J. Parviainen and J. Collin, "Differential barometry in personal navigation," in *Proc. of 2008 IEEE/ION Position, Location and Navigation Symposium*, Monterey, CA, May 2008, pp. 148–152.

[15] "BMP085 digital pressure sensor data sheet," Bosch Sensortec, Oct. 2009.

[16] M. D. Shuster, "A survey of attitude representations," *The journal of the Astronautical Sciences*, vol. 41, no. 4, pp. 439–517, Oct. 1993.

[17] J. R. Magnus and H. Neudecker, *Matrix Differential Calculus with Applications in Statistics and Econometrics*. John Wiley & Sons, 1999.